RSC Sustainability

ROYAL SOCIETY OF CHEMISTRY

PAPER

View Article Online
View Journal | View Issue

Cite this: *RSC Sustainability*, 2026, **4**, 1097

Microwave-assisted green synthesis of ZnO nanoparticles utilizing *Litchi chinensis* leaf waste for the efficient photocatalytic degradation of methylene blue

Mofassel Hossen Akash, Shukanta Bhowmik, Md. Abdus Samad Azad, Nahid Sultana and Md. Ashraful Alam *

The accumulation of fruit residues contributes significantly to environmental pollution, prompting extensive research aimed at managing this waste while generating economic value. In this context, the present study introduces a novel method for the utilization of litchi leaf waste through a green route to synthesize ZnO nanoparticles. This work focuses on a simple, eco-friendly, and energy-efficient approach in which litchi leaf extract functions simultaneously as the reducing, capping, and stabilizing agent during nanoparticle formation. The objective is to develop a non-toxic, facile and sustainable approach for fabricating photocatalytically active ZnO nanoparticles and evaluating their efficiency in degrading methylene blue dye. Additionally, the effect of varying microwave power levels on the characteristics of the nanoparticles is examined. The synthesized ZnO nanoparticles were characterized through XRD, UV–vis spectroscopy, SEM, EDX spectroscopy, and FTIR spectroscopy to analyze their crystallite size, optical property, morphology, elemental composition, and functional groups, respectively. XRD analysis verified the formation of hexagonal wurtzite ZnO with an average crystallite size of 17.76 nm according to the Scherrer equation. The UV–vis spectrum showed a prominent absorption wavelength at 374 nm, corresponding to a band gap energy of 3.33 eV. SEM micrographs showed uniformly distributed spherical nanoparticles, while EDX analysis confirmed that the material was of the highest purity, detecting only Zn and O. FTIR spectra confirmed the Zn–O stretching because of the presence of a characteristic peak at 664 cm^{-1}. The synthesized nanoparticles demonstrated promising photocatalytic activity under natural sunlight, achieving a 98% removal efficiency along with an adsorption capacity of 49.4 mg g^{-1}, following first-order kinetics. However, increasing the microwave power resulted in reduced photocatalytic efficiency due to the promoted particle growth and enhanced agglomeration. Overall, the findings demonstrate that this green and sustainable synthesis approach provides efficient ZnO photo-catalysts suitable for wastewater treatment applications.

Received 10th December 2025
Accepted 8th January 2026

DOI: 10.1039/d5su00916b

rsc.li/rscsus

Sustainability spotlight

This work presents a sustainable pathway for nanomaterial synthesis by converting natural leaf waste into a valuable precursor for ZnO nanoparticle synthesis. The green method eliminates the use of toxic chemicals, such as NaOH, by employing plant extract as a natural reducing, stabilizing, and capping agent. The microwave-assisted process further enhances sustainability through reduced energy consumption. The resulting nanoparticles exhibit smaller crystallite size, minimal agglomeration, and excellent dye-degradation efficiency, enabling cleaner wastewater treatment. By promoting waste valorization, reducing chemical hazards, improving energy efficiency, and advancing eco-friendly remediation technologies, the study directly supports the UN Sustainable Development Goals, including SDG 6 (clean water and sanitation), SDG 7 (affordable and clean energy), SDG 12 (responsible consumption and production), and SDG 13 (climate action).

Introduction

In the past few years, rapid developments in the textile industry have led to severe environmental pollution, largely due to the excessive use of synthetic dyes. The major drawback of the large-scale use of synthetic dyes is the discharge of dye-containing effluents into water bodies during dyeing and processing operations.[1] These dyes are highly resistant to biodegradation and are not effectively removed by conventional water-treatment processes, remaining stable under exposure to temperature and light.[2] Among various dyes, methylene blue

Department of Applied Chemistry & Chemical Engineering, Noakhali Science and Technology University, Noakhali-3814, Bangladesh. E-mail: ashraf.acce@nstu.edu.bd

(MB) is particularly harmful because it is toxic, non-biodegradable, and persistent and can cause severe environmental and health impacts, including respiratory problems, skin irritation, and damage to aquatic life. Due to its widespread use in textiles and resistance to degradation, MB dye was selected as a model pollutant in this study to evaluate the photocatalytic efficiency of the synthesized ZnO nanoparticles.[3]

Developing advanced treatment technologies is essential to address the harmful impacts of persistent organic pollutants on living species. Among various water-treatment techniques, advanced oxidation processes (AOPs) are particularly effective for removing organic pollutants, especially recalcitrant compounds with low biodegradability. In this aspect, sunlight-assisted photocatalytic degradation using semiconductor-based photocatalysts offers an efficient solution.[4] When photocatalysts are irradiated with light of an appropriate wavelength (photon energy ($h\nu$) $\geq$ bandgap energy (E_g)), they absorb energy that excites electrons (e^-) from the valence band to the conduction band, generating positively charged holes (h^+) in the valence band. This photoexcitation produces high-energy e^-/h^+ pairs that migrate to the surface of the photocatalyst, where they initiate redox reactions to degrade organic pollutants.[5]

In the current conditions, there is an increasing demand for environmentally friendly methods to synthesize nanoparticles without relying on hazardous chemicals. Green synthesis using phytochemicals present in the plants has emerged as a promising alternative to traditional chemical routes, which are often expensive and unsustainable.[6] Interestingly, worldwide, large quantities of assorted fruit leaves are discarded in the environment during production and sale in the market. This fruit residue contributes to environmental pollution and clogs the drainage systems. Utilizing this leaf waste as an extract source provides an efficient and sustainable solution, as they can function as natural reducing, stabilizing, and capping agents for nanoparticle fabrication. Moreover, such benign biomaterials facilitate the production of biocompatible and eco-friendly nanoparticles, offering advantages such as minimal toxicity, cost-effectiveness, simplicity, reproducibility, and enhanced stability. Commonly available fruits in the market can be used in the synthesis of nanoparticles, including *Poncirus trifoliate*,[7] *Aloe vera*,[8] *Ziziphus jujuba*,[9] *Artocarpus heterophylus*,[10] guava,[11] *Cucumis melo*[12] and carambola.[13]

Various strategies have been employed to synthesize ZnO nanoparticles, such as solution precipitation,[14] hydrothermal,[15] CVD,[16] and sol–gel[17] methods, co-precipitation,[18] thermal decomposition,[19] ultrasound[20] and photochemical methods,[21] electrochemical reduction,[22] and microwave-assisted techniques.[23,24] Among these, microwave-assisted methods are particularly attractive as they are more energy-efficient, faster, less expensive, and require simpler equipment. Microwave irradiation enables high reaction rates, excellent selectivity, increased product yields, and uniform volumetric heating by directly heating the sample. Unlike conventional methods, microwave heating provides a uniform temperature distribution throughout the material, promoting rapid and uniform nanoparticle formation.[25]

Metal oxides with nanoscale morphologies (<100 nm) have gained significant attention in recent years, with ZnO nanoparticles standing out as a widely studied example. ZnO nanoparticles are n-type semiconductors with a high excitation energy (60 meV) and a wide band gap energy (3.37 eV) at room temperature. They are considered highly promising due to their cost-effectiveness, non-toxicity, high thermal and chemical stability, controllable resistance, piezoelectric behavior, large quantum field, versatile morphologies, and excellent electrical and optical characteristics.[26,27] These features have driven advances in diverse fields such as agriculture,[28] biomedicine,[29,30] catalysis,[31] coatings,[32] the cosmetic industry,[33] drug delivery,[34] electronics and energy,[35] sensors,[36] mechanics,[37] optics and the space industry,[38] anti-microbiotics,[39] antibacterials,[40–42] antioxidants[43,44] and diabetic treatment.[45]

This experiment aimed to synthesize ZnO nanoparticles using an eco-friendly route based on abundantly available "*Litchi chinensis*" leaf waste extract as a reducing, capping and stabilizing agent under microwave irradiation, to evaluate their photocatalytic efficiency against the most prevalent methylene blue dye under sunlight. Additionally, the photocatalytic activity of the synthesized nanoparticles at diverse microwave power levels was compared. For this purpose, the nanoparticles were characterized using X-ray diffraction (XRD), ultraviolet-visible (UV-vis) spectroscopy, scanning electron microscopy (SEM), energy-dispersive X-ray spectroscopy (EDX), and Fourier-transform infrared spectroscopy (FTIR).

Materials and methods

Materials

Leaves of *Litchi chinensis* were obtained from a local bazaar in Noakhali, and distilled water was used during the experiments. Zinc nitrate hexahydrate [$Zn(NO_3)_2$ $6H_2O$] and methylene blue dye were procured from Sigma-Aldrich, with all chemicals being analytical grade. Prior to use, all glassware was sterilized, and all instruments were calibrated. The synthesis was performed in a microwave oven (IBF 20 L-20PM-MEC2) with adjustable power settings to achieve uniform heating.

Methods

Preparation of leaf extract. Leaves were thoroughly washed with deionized (DI) water and air-dried in the dark at ambient temperature. After a few days, the dried leaves were ground into powder. Approximately 50 g of the leaf powder was mixed with 200 mL of DI water in a 250 mL beaker. The mixture was warmed on a hot plate at 70 °C for 60 min. Afterward, the mixture was allowed to cool at ambient temperature and screened using Whatman filter paper. Finally, the resulting filtrate solution was stored at 4 °C in a refrigerator.

Preparation of ZnO nanoparticles *via* microwave-assisted green synthesis. 200 mL of the leaf extract was mixed with 100 mL of a 0.1 M zinc nitrate hexahydrate solution, placed on a magnetic stirrer, and stirred continuously at 800 rpm at ambient temperature for 30 minutes to promote interaction between the metal ions and the plant-derived phytochemicals.

After uniform mixing, 90 mL of the resulting solution was divided into three equal portions. These samples were irradiated in a microwave at power levels of 400 W, 500 W, and 600 W for 5 minutes at 30 °C in intermittent cycles (60 seconds on, 30 seconds off) to ensure uniform energy distribution and prevent overheating. Microwave exposure accelerated the nucleation and crystal formation of the nanoparticles. After irradiation, the homogeneous mixture was cooled to ambient temperature, forming a brown precipitate, which was collected by centrifugation at 8000 rpm for 30 minutes, and washed 3 times with deionized water to remove residual phytochemicals and ionic impurities. The precipitate was then dried in an oven at 60 °C for 1 h and finally calcined in a muffle furnace at 500 °C for 3 hours to enhance crystallinity and eliminate remaining organic matter. The final white ZnO nanoparticles were stored in an airtight glass vial for characterization and application. To verify the reproducibility, this experimental procedure was repeated three times under the same conditions, yielding consistent results and confirming the reliability of the method. The efficiency of the microwave-assisted green synthesis was determined by calculating the yield of the resulting ZnO nanoparticles using the following equation:

$$\text{Yield}(\%) = \left(\frac{\text{Weight of dried ZnO NPs}}{\text{Theoretical weight of precursor Zn salt}}\right) \times 100 \quad (1)$$

In this process, 2.9749 g of zinc salt was used as the precursor, yielding 2.8323 g of ZnO nanoparticles, which corresponds to a yield efficiency of 95.21%. A schematic of the overall synthesis process is shown in Fig. 1.

Characterization of the synthesized ZnO nanoparticles

Optical analysis. The absorption spectrum of the synthesized nanoparticles was measured over the 200–700 nm range with a LAMBDA®365+ double-beam UV-visible spectrophotometer, with deionized water as a reference solvent. To measure the optical parameters, 0.01 g of nanoparticles was ultrasonically dispersed in 10 mL of deionized water to ensure a uniform suspension. The band gap energy offers valuable information about the electronic structure and potential applications in optoelectronic and photocatalytic activity. The energy gap was measured by using the following equation:

$$E = hc/\lambda \quad (2)$$

The value of Planck's constant (h) is 4.1361×10^{-15} eV s, the speed of light (c) is 3×10^{8} m s^{-1}, and the peak absorbance wavelength (λ) is in nm. So, the above equation becomes:

$$E_g = 1239.83/\lambda \text{ nm} \quad (3)$$

Here, E_g denotes the optical band gap energy in electron volts (eV). The energy gap of the ZnO nanoparticles was determined using the Tauc relation, which is given by the following equation:

$$(\alpha h\nu)^n = D\,(h\nu - E_g) \quad (4)$$

In this equation, D is a constant, α represents the absorption coefficient, E_g denotes the optical band gap, and $h\nu$ refers to the photon energy. The parameter n indicates the type of electronic transition, which is 2 for a direct allowed transition.

FTIR analysis. FTIR spectra of the nanoparticles were obtained using an FTIR spectrometer (PerkinElmer Spectrum Two™ IR spectrometer) to identify functional groups and chemical bonds over the wavenumber range of 400 to 4000 cm^{-1}.

SEM imaging. The surface morphology and particle size of the nanoparticles were examined using a ZEISS Sigma SEM operated at an accelerating voltage of 10 kV. Particle diameter was

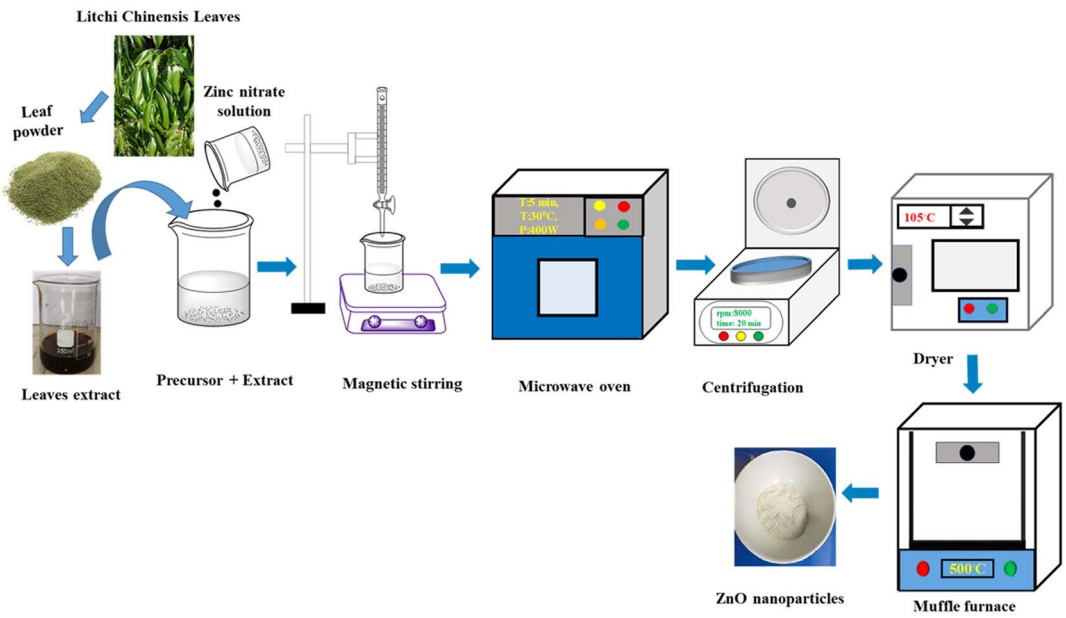

Fig. 1 Schematic representation of microwave-assisted synthesis of ZnO nanoparticles using litchi leaf extract.

measured using ImageJ software. For elemental composition and purity assessment, the samples were placed on a copper grid and analyzed using energy-dispersive X-ray (EDX) spectroscopy. Before SEM and EDX measurements, the nanoparticles were dried in a vacuum dryer at 50 °C overnight to remove residual moisture.

XRD analysis. XRD analysis was performed to assess the crystallite size, phase purity and structural integrity of the prepared nanoparticles. This measurement was performed using a high-precision diffractometer operating at 40 kV and 30 mA, with Cu-Kα radiation ($\lambda = 1.5406$ Å). Scanning was carried out across a 2θ range of 5–80°, providing a comprehensive evaluation of the lattice structure and phase content of the nanoparticles.

Photocatalytic degradation of MB dye

The photocatalytic activity of the synthesized ZnO nanoparticles was assessed through the sunlight-driven degradation of MB dye. In this experiment, 5 mg of ZnO nanoparticles were dispersed in 40 mL of a 5 ppm MB solution. Before exposure to sunlight, the dispersion was magnetically stirred in the dark for 30 minutes to achieve adsorption–desorption equilibrium. During the photo-catalysis, at 20-minute intervals, a 3 mL aliquot of the dispersion was withdrawn and centrifuged. The absorbance of the clear supernatant was analyzed using a UV–visible spectrometer. The residual MB dye concentration was determined by measuring absorbance at 664 nm and converting it into concentration using the standard calibration curve. The degradation efficiency, rate of degradation and adsorption capacity were calculated using eqn (5)–(7), respectively.

$$\%\ \text{Degradation} = \frac{A_0 - A}{A_0} \times 100 \tag{5}$$

$$\ln\left(\frac{A}{A_0}\right) = -kt \tag{6}$$

$$\text{Adsorption capacity, } q_e = \frac{(C_0 - C) \times V}{W} \tag{7}$$

In eqn (5) and (6), A_0 and A represent the initial and final absorbance of the MB dye solution, respectively. The constant k represents the reaction rate of the degradation process. In eqn (7), C_0 and C indicate the first and last concentrations of MB dye in ppm, respectively, while V denotes the volume of the dye solution (in liters), W is the mass of the dry ZnO (in grams), and k is the rate constant of the reduction reaction. The time needed for 50% dye degradation (T_{50}) was determined using eqn (8).

$$T_{50} = \frac{0.693}{k} \tag{8}$$

To assess the photocatalytic performance of the ZnO nanoparticles, the absorbance of the MB dye solution was measured without sunlight irradiation as a control.

Reusability test. A reusability study of the prepared ZnO nanoparticles (400 W, 500 W, 600 W) was conducted to monitor the degradation of MB dye solutions over five consecutive cycles under the same conditions (5 mg of ZnO and 40 mL of 5 ppm dye solution). After each experiment, the ZnO photo-catalyst was recovered and thoroughly washed with distilled water and 10% ethyl alcohol to remove remaining organics. The samples were then centrifuged (20 min) and dried (60 °C, 6 h) before reuse in the next cycle. Finally, photocatalytic measurements were conducted according to the experimental procedure discussed in the earlier section.

Radical scavenger identification test

Scavenging activity assays were carried out to determine the primary reactive oxygen species (ROS) responsible for the photocatalytic degradation of MB dye using ZnO nanoparticles under sunlight. Different scavengers were used, including EDTA (0.1 M, 1 mL) for capturing generated holes (h^+), isopropanol (0.1 M, 1 mL) for hydroxyl ($OH^\bullet$), and silver nitrate (0.1 M, 1 mL) for superoxide radicals ($^\bullet O_2^-$). The experiment was carried out under identical conditions (5 mg ZnO, 5 ppm dye). The three synthesized ZnO nanoparticle samples (400 W, 500 W, and 600 W) were exposed to UV light for 40 minutes in the presence of each scavenger. After irradiation, the solution was centrifuged to remove ZnO nanoparticles, and the absorbance was measured.

Result and discussion

Synthesis of ZnO nanoparticles using *Litchi chinensis* leaf extract under microwave heating

Various phenolic phytochemicals, including flavonoids and condensed tannins present in the *Litchi chinensis* leaf extract, acted as reducing, capping and stabilizing agents during the formation of the nanoparticles.[46] There are two proposed explanations for the formation of ZnO nanoparticles using the aqueous leaf extract: In the first pathway, when zinc salt was mixed with the leaf extract under specific reaction conditions, the Zn^{2+} ions form complexes with the phytochemicals present in the extract. These complexes then react with hydroxide ions (OH^-) supplied by the phenolic group in the extract to form a precipitate (ppt.) of $Zn(OH)_2$. Simultaneously, phytochemicals present in the extract were able to reduce Zn^{2+} ions to zero-valent zinc (Zn^0), which subsequently reacts with dissolved oxygen (DO) to generate the ZnO nuclei. Additionally, the phytochemicals cap these nuclei and prevent agglomeration of the ZnO nanoparticles by stabilizing them.

$$Zn(NO_3)_2 \cdot 6H_2O + \text{aqueous leaves extract} \rightarrow ZnO + 2NO_3^- + 6H_2O + \text{other products}$$

In the second pathway, when the zinc nitrate hexahydrate solution is mixed with the leaf extract, a light-brown ppt. of $Zn(OH)_2$ forms immediately. The resulting solution is then irradiated in a microwave oven, which facilitates the transformation from $Zn(OH)_2$ to ZnO nanoparticles.[47] After microwave irradiation, brown precipitates formed due to interactions between the metal ions and the phytochemicals, verifying the formation of ZnO nanoparticles. Thereafter, the ppt. is calcined

in a furnace to remove organic impurities, yielding white ZnO nanoparticles. The microwave radiation supplies the energy needed for initiating and accelerating the reaction, and helps control the particle size. In this route, Zn^{2+} ions from the zinc nitrate solution are reduced and stabilized through complexation with phytochemicals present in the leaf extract. In the aqueous media, the anionic part of the zinc precursor salt is excluded as the acid by accepting protons from the leaves' phyto-chemicals, while water molecules contribute protons to the phytochemicals as well. Simultaneously, hydroxyl groups in the solution, from phytochemicals react with the stabilized metal species to form $Zn(OH)_2$. All these steps occur simultaneously, and the resulting mixture is oven-dried to yield light-brown particles, which are then calcined to remove residual hydroxides and impurities, producing the final ZnO nanoparticles (Fig. 2).

$$Zn(NO_3)_2 \cdot 6H_2O + \text{aqueous leaves extract} \rightarrow [Zn(\text{phytochemicals})_2]^{2+} + 2NO_3^- + 6H_2O$$

$$[Zn(\text{phytochemicals})_2]^{2+} + 2OH^- \rightarrow Zn(OH)_2\downarrow + 2\ \text{Phytochemicals}$$

$$Zn(OH)_2 \xrightarrow{\Delta} ZnO + H_2O(g)$$

Crystallographic analysis

Fig. 3 presents the XRD patterns of the synthesized ZnO samples (400 W, 500 W and 600 W). Table 1 shows the diffraction angle (2θ) corresponding to the planes for the samples prepared at 400 W, 500 W and 600 W. Similar diffraction peaks are indexed by JCPDS card no. 96-900-4182, confirming the single-phase hexagonal wurtzite pattern in all the nanoparticle samples. The absence of any additional peaks further indicates that no impurities, secondary phases, or by-products were generated during the synthesis. The average crystallite size for each sample was determined using the Scherrer equation (eqn (9)).

$$D = \frac{K\lambda}{\beta \cos \theta} \quad (9)$$

In this equation, D, K, λ, θ and β represent the crystalline size, the Scherrer constant (0.9), the wavelength, the Bragg angle, and the full width at half maximum (FWHM) of the diffraction.

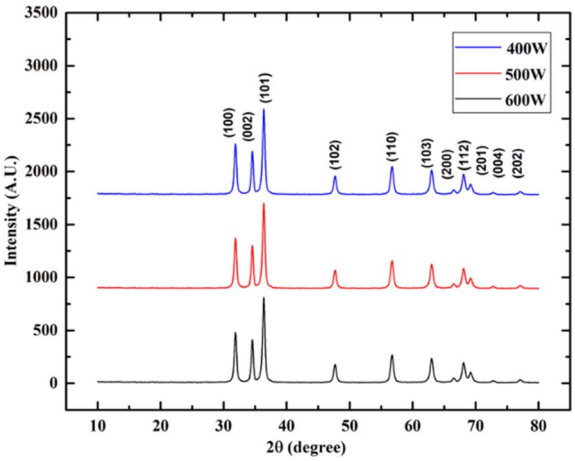

Fig. 3 XRD patterns of 400 W, 500 W and 600 W ZnO nanoparticles.

$$\text{Microstrain}, \varepsilon = \frac{\beta}{4 \tan \theta} \quad (10)$$

Microstrain refers to the degree of distortion or internal stress present within the crystalline lattice of a material and is given by the formula shown in eqn (10). The relationship between microstrain and crystallite size is often an inverse one: typically, smaller crystallites are associated with higher microstrain values. Crystallite dislocations generated by microstrain can significantly influence the material's overall behavior and performance. High microstrain often arises from high dislocation densities and grain boundaries, which impede the movement of dislocations. This phenomenon, known as work hardening or strain hardening, increases the material's yield strength and overall hardness.

$$\text{Dislocation density}, (\delta) = \frac{1}{D2} \quad (11)$$

Dislocation density is a key structural parameter that quantifies the total length of dislocations per unit volume within a crystallite; a higher dislocation density is generally associated with increased crystallite strength and hardness. The magnitude of line dislocation was determined using eqn (11). The calculated crystallite size, microstrain, crystallinity index and dislocation density are listed in Table 2. Among the samples,

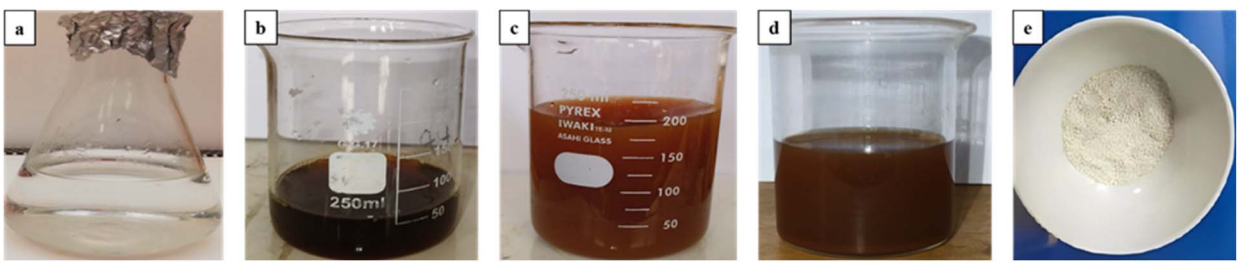

Fig. 2 Images of (a) zinc nitrate hexahydrate precursor, (b) leaf extract, and sample (c) before and (d) after microwave radiation, and (e) white ZnO nanoparticles.

Table 1 Crystallographic properties of the ZnO nanoparticles

ZnO nanoparticles	2θ (°)	FWHM (β) (°)	Miller plane (*hkl*)	Crystallite size (nm)	Microstrain (ε)	Dislocation density (δ)
400 W	31.70	0.46222	(100)	17.87	0.00649	0.00313
	34.37	0.41347	(002)	20.11	0.00583	0.00247
	36.17	0.47979	(101)	17.42	0.00837	0.00330
	47.45	0.53206	(102)	16.31	0.00528	0.00376
	56.52	0.57574	(101)	15.67	0.00469	0.00407
	62.77	0.61368	(103)	15.16	0.00439	0.00435
	66.30	0.64609	(200)	14.69	0.00432	0.00463
	67.87	0.63764	(112)	15.02	0.00413	0.00443
	69.02	0.69172	(201)	13.94	0.00439	0.00515
	72.52	0.34322	(004)	28.71	0.00204	0.00121
	76.87	0.49460	(202)	20.51	0.00272	0.00238
500 W	31.89	0.41886	(100)	19.77	0.00639	0.00256
	34.58	0.37247	(002)	22.37	0.00522	0.00200
	36.37	0.41826	(101)	20.00	0.00555	0.0025
	47.71	0.44663	(102)	19.48	0.00441	0.00264
	56.71	0.51756	(101)	17.46	0.00418	0.00328
	62.89	0.48089	(103)	19.40	0.00343	0.00266
	66.43	0.38087	(200)	24.99	0.00254	0.00160
	68.03	0.55078	(112)	17.43	0.00356	0.00329
	69.11	0.69089	(201)	13.98	0.00438	0.00512
	72.68	0.43007	(004)	22.94	0.00255	0.00190
	77.01	0.57027	(202)	17.81	0.00313	0.00315
600 W	31.71	0.29808	(100)	27.71	0.00458	0.00130
	34.36	0.30362	(002)	27.44	0.00429	0.00132
	36.18	0.32075	(101)	26.12	0.00429	0.00147
	47.52	0.34121	(102)	25.45	0.00338	0.00154
	56.51	0.36213	(101)	24.91	0.00294	0.00161
	62.75	0.42449	(103)	21.95	0.00303	0.00208
	66.34	0.37040	(200)	25.65	0.00247	0.00152
	67.84	0.44243	(112)	21.66	0.00287	0.00213
	69.01	0.48010	(201)	20.08	0.00305	0.00248
	72.46	0.40060	(004)	24.62	0.00239	0.00165
	76.80	0.44003	(202)	23.04	0.00242	0.00188

Table 2 Average crystal parameters for the ZnO nanoparticles

ZnO nanoparticles	Crystallite size (Scherrer equation) (nm)	Crystallite size (W–H equation) (nm)	Microstrain (ε)	Dislocation density (δ)
400 W	17.76	17.80	0.00479	0.0035
500 W	19.60	24.80	0.00412	0.0027
600 W	24.42	36.50	0.00326	0.0017

the 600 W sample exhibits the largest crystallite size, whereas the 400 W sample shows the smallest, indicating that the choice of microwave power significantly affects ZnO crystal growth. A previous study also reported that the crystallite size varies with the microwave power during synthesis. It is well established that a decrease in crystallite size results in an increase in surface area and defect sites, promotes charge carrier separation, and reduces recombination. As a result, photocatalytic efficiency is enhanced. Based on these findings, sample 400 W demonstrates the smallest crystalline size and superior catalytic efficiency compared to the other samples.

The Scherrer equation only considers crystallite size and does not reflect other intrinsic lattice imperfections, such as defects, stacking faults, grain boundaries, or lattice strain.[48,49] Because these structural features also contribute to peak broadening in XRD patterns, the Williamson–Hall (W–H) approach was developed to simultaneously assess crystalline dimensions and lattice strain, both of which influence strain-induced broadening.[50] In this model, the overall peak broadening is expressed as the combined effects of size and strain:

$$\beta_{\text{total}} = \beta_{\text{size}} + \beta_{\text{strain}} \quad (12)$$

According to the Stokes and Wilson formula, strain-related broadening is given by:

$$\beta_{\text{strain}} = 4\varepsilon \tan\theta \quad (13)$$

Meanwhile, rearranging the Scherrer equation gives the size-dependent broadening:

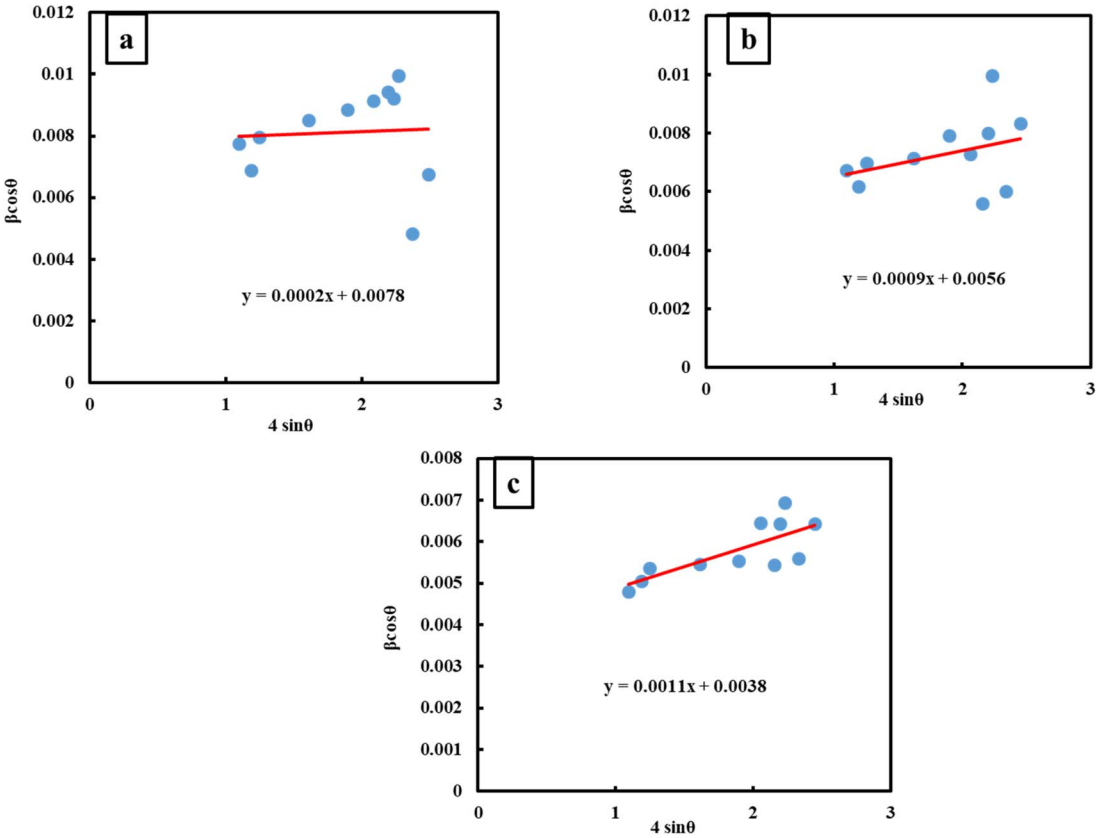

Fig. 4 W–H scheme for ZnO nanoparticles at (a) 400 W, (b) 500 W, and (c) 600 W.

$$\beta_{size} = \frac{K\lambda}{D\ \cos\ \theta} \quad (14)$$

Thus, crystallite-size broadening varies with cosθ, whereas strain-related broadening varies with tanθ. The uniform deformation method (UDM) is a simplified version of the W–H model that assumes uniform strain throughout the crystal and isotropic deformation. Under these assumptions, the total broadening becomes:

$$\beta_{total} = \frac{K\lambda}{D\ \cos\ \theta} + 4\varepsilon\ \tan\ \theta \quad (15)$$

Multiplying both sides by cosθ yields the linear form:

$$\beta_{total}\cos\ \theta = \frac{K\lambda}{D} + 4\varepsilon\ \sin\ \theta \quad (16)$$

Here, β_{total} illustrates the FWHM of the pattern, θ represents the Bragg angle, K is the shape constant (usually 0.9), λ denotes the X-ray diffraction wavelength, D corresponds to the crystal size, and ε indicates the microstrain. To extract the crystal size and lattice strain, a plot of 4sinθ (x-axis) *versus* β_{total} cosθ (y-axis) is constructed (Fig. 4). The crystal size is obtained from the intercept by implementing in $\frac{K\lambda}{D}$, whereas the slope provides

Table 3 Comparative XRD analysis of *Litchi chinensis*-based ZnO nanoparticles produced in this study with other plant-extract-based ZnO nanoparticles

No	Synthesis method	Plant extract	Crystallite size, (nm)	Applications	Reference
1	Green synthesis	*Allium cepa* L.	57	Antioxidant, antibacterial	53
2	Biosynthesis	*Eclipta prostrata*, *Piper longum*	17–30	Antioxidant, antibacterial, photocatalytic	54
3	Green synthesis	*Padina pavonica*	35.89	Photocatalytic	55
4	Chemical synthesis	—	45.5, 47.7, 37.5	Photocatalytic	56
5	Biosynthesis	*Sorghum panicle*	59.49	Photocatalytic	57
6	Green synthesis	*Ocimum basilicum* L.	30.39	Paracetamol removal	58
7	Biosynthesis-microwave	*Ziziphus jujuba*	25	Photocatalytic	9
8	Microwave-green synthesis	*starch*	24.41	Antibacterial, photocatalytic	23
9	Green-microwave synthesis	*Litchi chinensis*	17.76, 19.60, 24.42	Photocatalytic	Present study

the strain value. In Fig. 4, for the 400 W sample, the W–H plot revealed a linear relation expressed as $y = 0.002x + 0.0078$. The slope of 0.002 corresponds to the microstrain, indicating low lattice distortion in the synthesized ZnO nanoparticles. Using the intercept value of 0.0078, the crystal size was determined to be 17.8 nm. A higher slope indicates a greater lattice strain in the structure; in contrast, a larger intercept signifies a smaller crystal size. On the other hand, the 500 W and 600 W samples gave linear equations $y = 0.0009x + 0.0056$ and $y = 0.0011x + 0.0038$, respectively. The slopes correspond to microstrain values of 0.0009 and 0.0011, respectively, which are both very low, indicating minimal lattice distortion. Using the intercepts, the crystallite sizes are 24.8 nm and 36.5 nm, respectively. Typically, the crystallite size predicted by UDM is larger than that estimated using the Scherrer equation alone. This difference arises because β_{strain} and ε are estimated indirectly rather than measured directly from XRD data. The slope's sign also represents the type of strain in the crystal: positive and negative slopes indicate tensile and compressive strain, respectively.[51,52]

A comparative review (Table 3) of ZnO nanoparticle synthesis methods reveals significant variations in crystallite size depending on plant sources and synthesis method. Notably, the present experiment using the extract from *Litchi chinensis* leaves through a green and microwave-assisted route achieved the smallest crystallite sizes (17.76–24.42 nm), confirming its potential as a promising phyto-reductant for producing highly active photocatalytic ZnO nanoparticles.

Optical property analysis

The UV–visible spectrum was used to examine the absorption behavior of the synthesized ZnO nanoparticles and to calculate their energy band gap. The samples (400 W, 500 W, and 600 W) were examined over a wavelength range of 200–700 nm, and the energy gap was determined from the Tauc plot. Fig. 5(a) displays the recorded absorbance spectrum, while Fig. 5(b) shows the corresponding Tauc plot. The maximum absorption peaks appeared at 374 nm for the 400 W sample and at 377 nm for both the 500 W and 600 W samples. These absorption peaks are attributed to the intrinsic band–gap transitions, surface plasmon resonance, and quantum confinement effects. The narrow absorption peaks at 374 nm and 377 nm align well with previous reports.[59] The estimated optical energy difference was approximately 3.32 eV (400 W), 3.33 eV (500 W), and 3.33 eV (600 W), which fall within the typical range reported for ZnO nanoparticles (3.10–3.37 eV).[60] The slight red shift in the absorption edge for the 500 W and 600 W samples is attributed to their larger particle sizes compared to the 400 W sample.[61] Furthermore, the presence of sharp, intense peaks without additional secondary absorption peaks confirms the highest integrity of the prepared ZnO nanoparticles. For the Tauc plot, $(\alpha h\nu)^2$ was plotted against $(h\nu)$, assuming a direct allowed transition.

Morphology analysis. SEM analysis was conducted to examine the morphology of the ZnO nanoparticles, as these characteristics are crucial for defining the surface properties of a material and assessing its potential applications. Fig. 6(a–c) shows the SEM micrographs of the prepared ZnO nanoparticles (400 W, 500 W and 600 W). The images reveal that all the nanoparticles possess homogeneous spherical shapes with regular and rounded forms. Nevertheless, differences in particle size became apparent with changes in microwave power. The 400 W sample exhibited well-dispersed particles, whereas higher microwave powers (500 W and 600 W) resulted in noticeable particle aggregation, as indicated in Fig. 6(a–c). Particle size distribution histogram data further showed that the average particle sizes were 722 nm, 865 nm, and 951 nm for the 400 W, 500 W, and 600 W samples, respectively. This size increase with increasing microwave power is consistent with previously reported findings.[62] As the microwave power increases, the temperature rises because higher power supplies more energy within the same time, resulting in a faster heating rate. Under these conditions, Ostwald ripening takes place: smaller particles, which possess higher surface energy and therefore higher solubility, begin to dissolve more readily in the surrounding medium. With the added thermal energy, particles gain greater kinetic motion and diffuse more rapidly through the solution. The dissolved species then redeposit onto the surfaces of larger, more stable crystals, which have lower surface energy, causing them to grow further. However, the

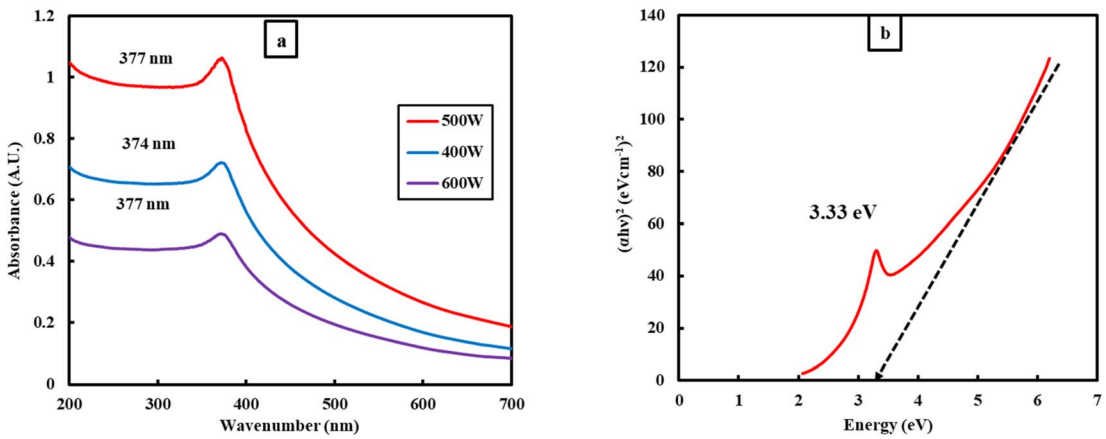

Fig. 5 (a) UV-visible spectra of the 400 W, 500 W and 600 W samples. (b) Tauc plot of ZnO nanoparticles.

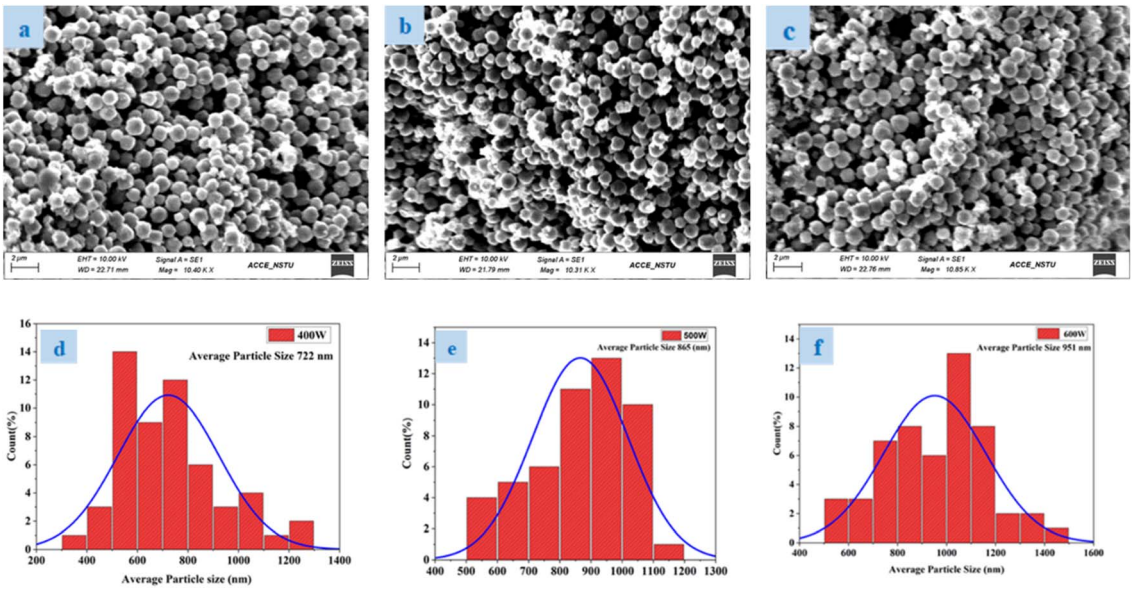

Fig. 6 (a–c) SEM images of the 400 W, 500 W, and 600 W samples. (d–f) Particle size distribution graphs for the 400 W, 500 W, and 600 W samples.

findings from the SEM analysis reveal that all the ZnO nanoparticle samples possess homogeneous, spherical, and regularly rounded shapes. The spherical morphology of ZnO nanoparticles provides several functional benefits, such as maximum surface area/volume percentage, increased number of active surface sites, uniform light scattering, enhanced light absorption, and a consistent isotropic nature.[63–65] Additionally, spherical particles disperse more evenly in solution, reducing aggregation and improving overall stability. This geometry also facilitates easier recovery and reuse through uniform settling or filtration. Collectively, these features contribute to efficient charge separation, increased generation of reactive species, and improved reliability in dye degradation processes.

Elemental composition analysis. The atomic composition in the ZnO nanoparticles was examined using EDX spectroscopy, as this information is crucial for understanding the material's characteristics and evaluating its suitability for diverse applications. The EDX spectra, shown in Fig. 7(a–c), of the prepared ZnO nanoparticles displayed a strong, sharp primary peak for zinc and an intense, well-defined oxygen peak. The clear and distinct peaks, without any additional signals, confirm the presence of only zinc and oxygen elements, indicating high chemical purity and successful formation of ZnO nanoparticles free from detectable impurities. Table 4 showed that, relative weight percentages of zinc to oxygen were 66.37 : 33.63, 66.55 : 33.45, and 72.4 : 27.6 for 400 W, 500 W, and 600 W samples, respectively.[66] Corresponding relative atomic percentages were 32.56 : 67.44, 32.74 : 66.55, and 39.1 : 60.9 for the same samples. Ideally, stoichiometric ZnO should exhibit a theoretical weight ratio of approximately 80 : 20 and an atomic ratio of 50 : 50, reflecting its 1 : 1 composition. As microwave power increases from 400 W to 600 W, the higher energy input raises the temperature and accelerates particle growth through Ostwald ripening. This trend aligns with the EDX results, where

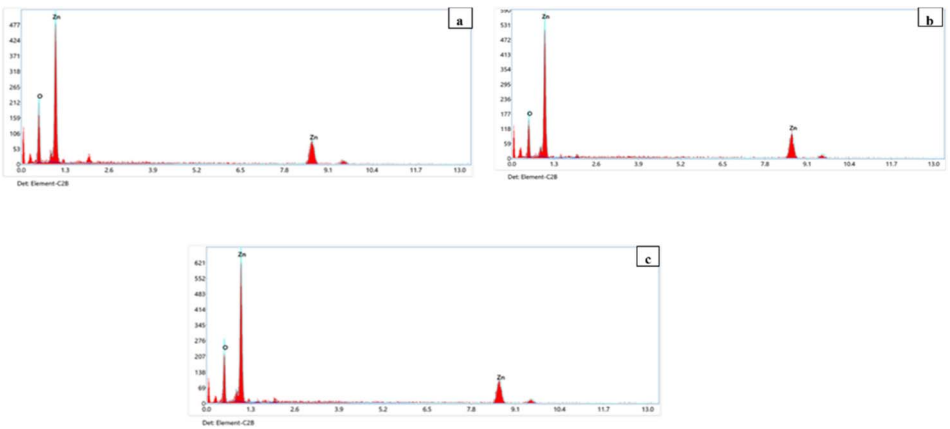

Fig. 7 Elemental composition spectra for ZnO nanoparticles at (a) 400 W, (b) 500 W and (c) 600 W.

Table 4 Elemental composition percentage of ZnO nanoparticles

	Sample					
	400 W		500 W		600 W	
Element	weight%	atomic%	weight%	atomic%	weight%	atomic%
Zn	66.37	32.56	66.55	32.74	72.4	39.1
O	33.63	67.44	33.45	66.55	27.6	60.9
Total	100					

the Zn content increases (from 66.37% to 72.40% by weight and from 32.56% to 39.10% by atomic percentage), indicating the formation of larger and more Zn-rich crystals. Higher thermal energy enables smaller ZnO nuclei to dissolve and redeposit onto larger, more stable crystals, resulting in particle growth and densification. Concurrently, the oxygen content decreases (from 33.63% to 27.60% by weight and from 67.44% to 60.90% by atomic percentage), reflecting the reduced presence of surface defects, oxygen-rich sites, and weakly adsorbed species, such as –OH groups and O_2, which are desorbed at elevated temperatures. Additionally, a smaller particle size (400 W) leads to a higher surface-to-volume ratio, enabling the nanoparticles to readily adsorb oxygen-containing species from the surrounding air or moisture, resulting in the formation of surface species, such as hydroxyl groups (OH^-), that contribute to the elevated oxygen signal in the spectrum.[67] Larger and smoother ZnO particles (600 W) also exhibit stronger Zn signals in the EDX spectrum, contributing to the observed compositional shift. The decrease in surface oxygen reduces electrostatic repulsion, while the larger particle size enhances attractive forces, collectively promoting agglomeration and potentially diminishing the catalytic activity of the ZnO nanoparticles. Overall, the EDX data demonstrate that higher microwave power enhances Zn-rich crystal growth, decreases surface oxygen, and increases particle agglomeration. Nevertheless, the clear elemental profiles and high purity confirm that the synthesized ZnO nanoparticles are well-suited for advanced applications in photo-catalysis and environmental remediation.

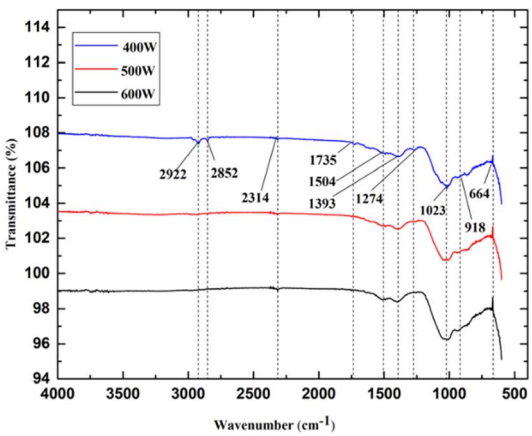

Fig. 8 Vibrational property analysis for 400 W, 500 W, and 600 W samples, respectively.

Vibrational properties analysis

The FTIR analysis provided additional confirmation of ZnO nanoparticle formation, as shown in Fig. 8. The absence of a strong broad absorption band at 3445 cm^{-1}, which corresponds to OH– bond stretching, indicates that the ZnO nanoparticles are free of residual moisture due to thorough drying in the vacuum dryer. A moderately intense peak at 2922 cm^{-1} corresponds to the C–H stretching mode of aliphatic groups, likely originating from residual organic constituents such as fatty acids, terpenoids, and waxes. Small peaks at 2314 cm^{-1} are commonly due to atmospheric CO_2 absorbed during the FTIR measurement. The peak at 1735 cm^{-1} corresponds to the C=O stretching mode, suggesting the presence of organic molecules such as lipids.[68,69] A minor peak at 1504 cm^{-1} indicates aromatic C=C stretching, pointing to the presence of residual aromatic phytochemicals including flavonoids and tannins. The band at 1393 cm^{-1} is assigned to C–O–H bending or symmetric carboxylate stretching, and the peak at 1274 cm^{-1} relates to the C–O vibration mode, reflecting alcohol, phenolic, or ether groups. The peak at 1023 cm^{-1} typically signifies the C–O functional group present in alcohols, ethers, esters, or carbohydrates.[70,71] The appearance of these organic groups indicates that the phytochemicals not only function as a reducing agent but also play a role in capping and stabilizing the nanoparticles. Finally, the strong vibration mode at 664 cm^{-1} is characteristic of Zn–O bonds, evidencing the composition of ZnO nanoparticles.[72] Overall, the FTIR spectra demonstrate the simultaneous presence of organic and inorganic functional groups, highlighting the successful attachment of phytochemicals to the ZnO nanoparticles. The metal–oxygen bonds confirm the function of phytochemicals in the effective synthesis of the nanoparticles.

Photocatalytic studies

Mechanism of photocatalytic activity of ZnO nanoparticles towards MB dye. The photo-driven degradation of MB dye by the ZnO catalyst proceeds through a free radical mechanism. During photo-catalysis, the free radicals produced in the aqueous media are highly responsive and attack the dye molecules, breaking them down into environmentally benign end products such as carbon dioxide (CO_2) and water (H_2O). The potential pathway for free radical formation by the ZnO catalyst in the presence of sunlight is illustrated in Fig. 9. Upon sunlight irradiation of the dye solution containing ZnO nanoparticles, electrons (e^-) in the photo-catalyst are excited from the valence band to the conduction band, leaving behind holes (h^+). These photogenerated charge carriers initiate a series of reactions

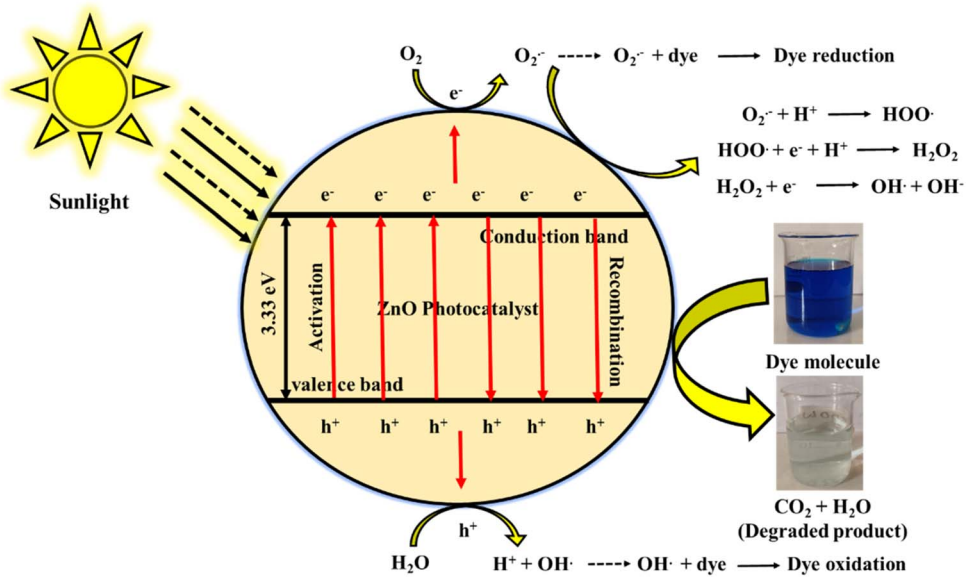

Fig. 9 Mechanistic pathway for the ZnO nanoparticle–assisted photo-degradation of MB dye.

responsible for radical formation. Electrons in the conduction band interact with oxygen molecules (dissolved or adsorbed) to form superoxide radical anion ($O_2^{\bullet -}$), while the valence band holes oxidize water molecules to produce protons (H^+) and hydroxyl radicals ($OH^\bullet$). Additionally, the holes may also react with surface-bound hydroxyl ions (OH^-) to produce more hydroxyl radicals. These primary radicals further participate in secondary reactions, forming other reactive oxygen species (ROS), including peroxide radicals ($HOO^\bullet$), hydroxyl radicals ($OH^\bullet$), and hydroxyl ions (OH^-). The superoxide and hydroxyl radicals serve as the main oxidizing agents that break down MB molecules through redox reactions, although secondary radicals also contribute to the overall degradation. Thus, the key factor driving dye decomposition is the formation of these reactive free radicals (h^+, $O_2^{\bullet -}$, $OH^\bullet$).[73] The principal steps involved in this mechanism are summarized as follows:

$$ZnO + h\nu \rightarrow ZnO\ (e_{(CB)}^-) + (h_{(VB)}^+) \quad \text{(i)}$$

$$h_{(VB)}^+ + H_2O \rightarrow H^+ + OH^\bullet \quad \text{(ii)}$$

$$e_{(CB)}^- + O_2 \rightarrow O_2^{\bullet -} \quad \text{(iii)}$$

$$O_2^{\bullet -} + H^+ \rightarrow HO_2^\bullet \quad \text{(iv)}$$

$$HO_2^\bullet + HO_2^\bullet \rightarrow H_2O_2 + O_2 \quad \text{(v)}$$

$$H_2O_2 + h\nu \rightarrow 2OH^\bullet \quad \text{(vi)}$$

$$\text{Organic pollutants} + OH^\bullet \rightarrow \text{Intermediates products} \rightarrow CO_2 + H_2O \quad \text{(vii)}$$

Effect of different microwave power levels on photocatalytic activity. The photocatalytic performance of the ZnO photocatalyst for the degradation of MB dye by ZnO-400 W, ZnO-500 W, and ZnO-600 W was evaluated, and the spectra are presented in Fig. 10(a–c). The photocatalytic efficiencies for the degradation of the samples were 98%, 90%, and 86%, respectively, indicating a steady decline in activity with increasing microwave power from 400 W to 600 W. The superior efficiency of ZnO-400 W is mainly due to its smaller particle size, which provides a larger number of active surface sites for charge transfer. However, as the particle size decreases, the likelihood of surface recombination increases because photogenerated carriers are produced closer to the surface, allowing recombination to compete more effectively with interfacial charge transfer.[67,74]

The initial enhancement in photo-catalysis activity may also be associated with a reduction in band gap, which facilitates greater charge-carrier generation.[75] Higher microwave power typically produces larger particles and may promote aggregation. Similarly, the elevated calcination temperatures enhance sintering, reducing the surface area and pore volume and thereby deactivating catalytic sites on the ZnO surface.[76] In this experiment, the energy gaps of the samples were calculated to be approximately 3.32, 3.33, and 3.33 eV for 400 W, 500 W, and 600 W samples, respectively. A lower band gap enables more charge carriers to participate in the photocatalytic process, contributing to higher degradation efficiency.[77] Kinetic analysis confirmed that MB degradation followed a first-order reaction.[78] The reaction rate constants under sunlight were 0.0295 min^{-1}, 0.0177 min^{-1}, and 0.0152 min^{-1} for ZnO-400 W, ZnO-500 W, and ZnO-600 W, respectively. ZnO-400 W showed the highest activity, acting 1.6 times faster than ZnO-500 W and 1.9 times faster than ZnO-600 W, and exhibited the shortest half-life (23.49 min). In contrast, none of the ZnO samples showed photocatalytic activity in the absence of sunlight, with only 12% of the dye degraded after 120 minutes (Fig. 10(d)). This indicates that ZnO nanoparticles require sunlight to function effectively as photo-catalysts for MB degradation. The reaction rate without sunlight was extremely low (0.0009 min^{-1}). Under

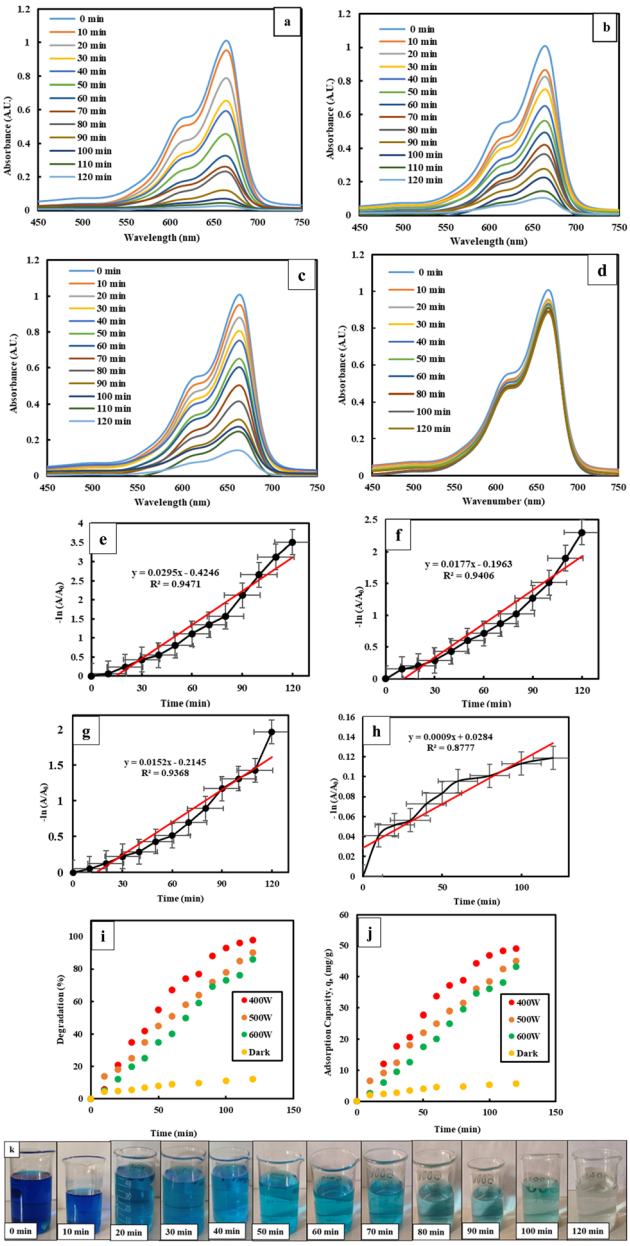

Fig. 10 UV-vis absorbance spectra showing the removal of MB dye by ZnO nanoparticles in the (a–c) presence of sunlight for 400 W, 500 W, and 600 W samples, respectively, and (d) in the absence of sunlight. (e–h) Plots of ln (A_t/A_0) *vs.* time, (i) degradation (%) *vs.* time, and (j) adsorption capacity (q_e) *vs.* time. (k) MB dye degraded over time by the ZnO photo-catalyst in the presence of light.

sunlight, the degradation proceeded approximately 33, 20, and 17 times faster for ZnO-400 W, ZnO-500 W, and ZnO-600 W, respectively, compared to that under dark conditions. The degradation efficiency and kinetic parameters of MB dye using synthesized ZnO at different microwave power levels are summarized in Table 5.

A comparison of photocatalytic degradation studies reveals notable differences in efficiency depending on the synthesis route, catalyst loading, and dye concentration (Table 6). Sol–gel-derived ZnO catalysts achieved efficiencies of 58–86% for methylene blue degradation at concentrations of 10–12 ppm, with rate constants of up to 0.010 min^{-1}. Biosynthesized and solution-combustion ZnO showed higher activity, reaching 92–94% degradation at 15 ppm within 120–180 minutes. In contrast, the present study employing a green microwave-assisted synthesis demonstrated superior photocatalytic performance at lower dye concentrations (5 ppm) and minimal catalyst dosage (0.1 g L^{-1}). The ZnO-400 W sample exhibited the highest efficiency (98%) with a reaction rate constant of 0.0295 min^{-1}, outperforming many conventional and green synthesis methods reported earlier. Meanwhile, ZnO-500 W and ZnO-600 W achieved 90% and 86% degradation, respectively, with slightly lower rate constants. These results highlight the advantages of microwave-assisted green synthesis in producing highly active ZnO photo-catalysts with enhanced reaction kinetics and efficient dye removal under mild conditions.

Reusability of the photo-catalyst

The recyclability of the prepared ZnO nanoparticles was assessed by monitoring the removal of MB dye over five consecutive reuse cycles, as illustrated in Fig. 11. The histogram shows that the ZnO photo-catalyst prepared at 400 W retained strong stability, achieving 98% degradation in the first cycle and 89% at the fifth cycle. Likewise, the 500 W and 600 W samples showed initial degradation efficiencies of 90% and 86%, which gradually decreased to 77% and 76% by the fifth cycle, respectively. This gradual decrease is likely due to catalytic poisoning, physical loss and agglomeration after each cycle. Catalytic poisoning occurs when residual dyes or intermediate degradation products accumulate on the catalyst surface *via* electrostatic interactions, van der Waals forces, or hydrogen bonding. This persistent adsorption shields active sites and obstructs light penetration, thereby suppressing the generation of reactive oxygen species and ultimately reducing photocatalytic efficiency. Simultaneously, nanoparticle agglomeration, driven by particle–particle interactions during recovery and drying cycles, further diminishes performance. This formation of larger aggregates reduces the effective surface area and hinders photon absorption through increased light scattering. These explanations are supported by experimental observations and literature reports.[36,84]

Radical scavenger identification tests

The scavenger test results (Fig. 12) showed that the 400 W sample achieved 98% dye degradation without any scavenger; this dropped to 5.28% with ethylene-diamine-tetra-acetic acid (EDTA), 45.13% with isopropyl alcohol (IPA), and 66.44% with silver nitrate ($AgNO_3$). Similarly, the 500 W sample degraded 97% of the dye in the absence of a scavenger, and decreased to 5.78%, 27.23%, and 75.55% in the presence of EDTA, IPA, and $AgNO_3$, respectively. For the 600 W sample, initial 95% removal declined to 5.55%, 31.35%, and 59.35% with EDTA, IPA, and $AgNO_3$, respectively. These results indicate that EDTA caused the most significant resistance to methylene blue dye degradation, highlighting the dominant role of photogenerated holes (h^+) during the photo-catalysis. On the other hand, $AgNO_3$,

Table 5 Photo-degradation percentages and kinetic evaluation of MB dye degradation using ZnO nanoparticles produced at different microwave irradiation powers

ZnO nanoparticles	Degradation (%)	Adsorption capacity (mg g^{-1})	Time (min)	Rate constant (k)	Half-life ($t_{1/2} = 0.693\ k^{-1}$) (min)	Regression coefficient (R^2)
400 W	98	49.1	120	0.0295	23.49	0.9471
500 W	90	45.1	120	0.0177	39.15	0.9406
600 W	86	43.3	120	0.0152	45.59	0.9368
Dark	12	5.7	120	0.0009	770	0.8777

Table 6 Comparison of the photocatalytic performance of the synthesized ZnO nanoparticles versus other reported ZnO nanoparticles for MB dye degradation under sunlight

Synthesis method	MB dye concentration (ppm)	Catalyst dosage (g L^{-1})	Photocatalytic efficiency (%)	Exposure time (min)	K (min^{-1})	R^2	Reference
Sol–gel	10	1	86	180	0.010	0.982	79
Sol–gel	12	2	58	120	—	—	80
Biosynthesis	15	1	92	120	0.022	—	81
Solution combustion	15	1	94	180	—	—	82
Green synthesis	10	1	75	180	0.008	—	83
Green synthesis	10	1	85.61	120	0.152	0.953	42
Green synthesis	10	1	82.2	120	0.015	0.981	78
Green-microwave synthesis	5	0.1	98	120	0.0295	0.947	Present study
			90		0.0177	0.941	
			86		0.0152	0.937	

which scavenges superoxide radicals ($^{\bullet}O_2^-$), showed a moderate effect, while IPA, targeting hydroxyl radicals ($^{\bullet}OH$), had the least impact on dye removal.

Perspective of the present study

The novelty of this study lies in the development of a rapid, eco-friendly, and cost-effective microwave-assisted green synthesis of ZnO nanoparticles using *Litchi chinensis* leaf waste, which eliminates the need for chemical reducing, stabilizing, or capping agents. This approach not only valorizes agricultural waste but also produces nanoparticles with uniform size, high purity, and superior photocatalytic activity, demonstrating enhanced efficiency in methylene blue degradation. Unlike conventional green synthesis methods, the combination of

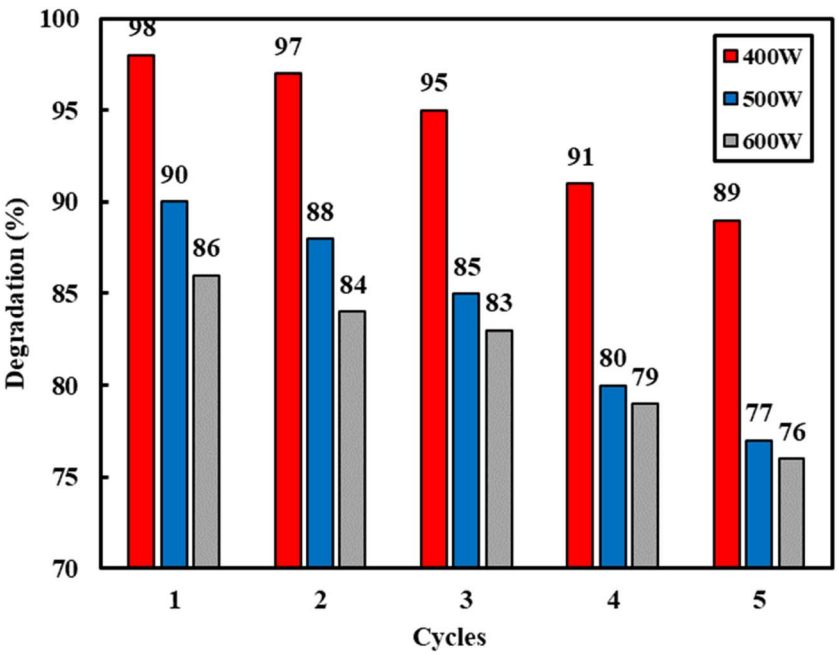

Fig. 11 Reusability of the three synthesized ZnO nanoparticle samples prepared at 400 W, 500 W, and 600 W.

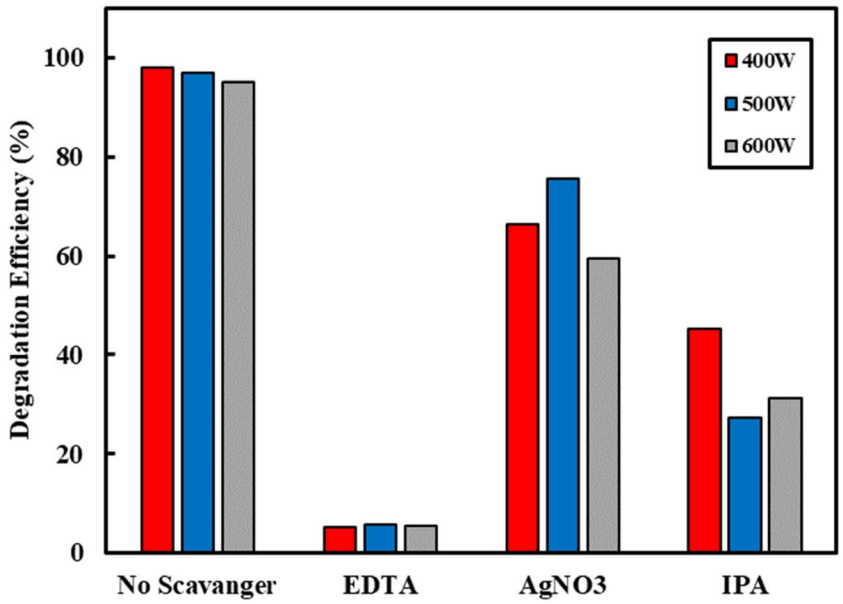

Fig. 12 Radical scavenger tests of the three synthesized ZnO nanoparticle samples prepared at 400 W, 500 W, and 600 W.

microwave irradiation and leaf waste extract ensures energy-efficient, scalable, and sustainable nanoparticle production, highlighting the study's novelty and practical relevance. Although the synthesized bio-fabricated ZnO nanoparticles offer several advantages as photocatalysts, including good reusability over multiple cycles, potential disadvantages include slight efficiency loss over repeated cycles due to catalytic poisoning or agglomeration. Immobilization on solid supports or heterojunction engineering can address these limitations and further enhance the durability and practical applicability.

Conclusion

In this experiment, ZnO nanoparticles were successfully synthesized *via* a microwave-assisted green route utilizing *Litchi chinensis* leaf waste extract as a natural phyto-reductant. This eco-friendly method minimized chemical usage and provided rapid, energy-efficient synthesis with controlled particle morphology. Structural characterization confirmed the formation of highly crystalline hexagonal ZnO with particle sizes ranging from 17.76 nm to 24.42 nm, with the smallest size observed at 400 W microwave power. Among the samples, ZnO-400 W exhibited the highest photocatalytic performance, achieving 98% degradation of methylene blue within 120 minutes under sunlight, compared to 90% and 86% for ZnO-500 W and ZnO-600 W, respectively. Kinetic analysis indicated first-order reaction behavior, with the fastest rate constant of 0.0295 min^{-1} for ZnO-400 W and a corresponding shortest half-life of 23.49 minutes. Reusability tests showed that ZnO-400 W retained 89% of its initial activity after five consecutive cycles. The present approach demonstrates promising scalability and cost-effectiveness due to the use of abundantly available *Litchi chinensis* leaf waste, the elimination of hazardous chemicals, and reduced energy consumption. The simplicity, environmentally benign nature, and economic viability of the approach reinforce its suitability for sustainable large-scale production. Overall, the findings highlight that the combination of *Litchi chinensis* leaf extract and microwave irradiation produces highly active, stable, and crystalline ZnO nanoparticles, demonstrating their strong potential for low-cost and sustainable wastewater treatment applications.

Author contributions

Mofassel Hossen Akash conceptualized, designed the experiment, performed data analysis, and contributed to the draft and final manuscript writing. Shukanta Bhowmik reviewed the draft version and assisted in preparing the final manuscript. Md. Abdus Samad Azad and Nahid Sultana assisted in drafting the manuscript. Md. Ashraful Alam supervised the entire project and coordinated and managed the necessary facilities.

Conflicts of interest

The authors declare that they have no conflicts of interest.

Data availability

The data that support the findings of this study are available from the corresponding author upon request.

Acknowledgements

This work was partially supported by the "Research Cell" at Noakhali Science and Technology University (NSTU) and the "Special Allocation for Science and Technology" under the Ministry of Science and Technology (MoST), Government of the People's Republic of Bangladesh. The authors gratefully

acknowledge the Department of ACCE, NSTU, Bangladesh, for support during this research.

References

1 M. Chen, Y. Shen, L. Xu, G. Xiang and Z. Ni, *Colloids Surf., A*, 2021, **613**, 126050.
2 J. Cheng, C. Zhan, J. Wu, Z. Cui, J. Si, Q. Wang, X. Peng and L.-S. Turng, *ACS Omega*, 2020, **5**, 5389–5400.
3 P. O. Oladoye, T. O. Ajiboye, E. O. Omotola and O. J. Oyewola, *Results Eng.*, 2022, **16**, 100678.
4 A. Fiszka Borzyszkowska, A. Pieczyńska, A. Ofiarska, W. Lisowski, K. Nikiforow and E. M. Siedlecka, *Int. J. Environ. Sci. Technol.*, 2020, **17**, 2163–2176.
5 S. R. D. Gamelas, J. P. C. Tomé, A. C. Tomé and L. M. O. Lourenço, *RSC Adv.*, 2023, **13**, 33957–33993.
6 C. Mallikarjunaswamy, V. Lakshmi Ranganatha, R. Ramu, U. C. Gowda and G. Nagaraju, *J. Mater. Sci.: Mater. Electron.*, 2020, **31**, 1004–1021.
7 P. C. Nagajyothi, T. N. Minh An, T. V. M. Sreekanth, J. Lee, D. Joo Lee and K. D. Lee, *Mater. Lett.*, 2013, **108**, 160–163.
8 G. Sangeetha, S. Rajeshwari and R. Venckatesh, *Mater. Res. Bull.*, 2011, **46**, 2560–2566.
9 M. N. Alharthi, I. Ismail, S. Bellucci, N. H. Khdary and M. Abdel Salam, *Nanomaterials*, 2021, **11**, 1682.
10 U. P. Manik, A. Nande, S. Raut and S. J. Dhoble, *Results Mater.*, 2020, **6**, 100086.
11 S. Mazhar, S. Hyder, B. S. Khan, A. S. Gondal, R. Ahmed, Iqra and M. Iqbal, *BMC Plant Biol.*, 2025, **25**, 499.
12 M. Shameem and W. Ahmad, *J. Inorg. Organomet. Polym.*, 2025, DOI: 10.1007/s10904-025-03942-x.
13 S. J. Mane Gavade, G. H. Nikam, R. S. Dhabbe, S. R. Sabale, B. V. Tamhankar and G. N. Mulik, *Adv. Nat. Sci.:Nanosci. Nanotechnol.*, 2015, **6**, 045015.
14 H. Ghorbani, F. Mehr, H. Pazoki and B. Rahmani, *Orient. J. Chem.*, 2015, **31**, 1219–1221.
15 S. S. Khudiar, F. A.-H. Mutlak and U. M. Nayef, *Optik*, 2021, **247**, 167903.
16 S. Stankic, S. Suman, F. Haque and J. Vidic, *J. Nanobiotechnol.*, 2016, **14**, 73.
17 A. B. Anik, M. Hossen Akash, Md. A. Alam, Md. Z. Alam, D. Sarker and N. Sultana, *RSC Adv.*, 2025, **15**, 45874–45888.
18 J. Kaewsaenee, M. T. Singhaset, K. Roongraung, P. Kemacheevakul and S. Chuangchote, *ACS Omega*, 2023, **8**, 43664–43673.
19 S. Hajiashrafi and N. Motakef Kazemi, *Heliyon*, 2019, **5**, e02152.
20 A. P. Nagvenkar, A. Deokar, I. Perelshtein and A. Gedanken, *J. Mater. Chem. B*, 2016, **4**, 2124–2132.
21 R. Joshi, *Materialia*, 2018, **2**, 104–110.
22 H.-D. So, S.-H. Jon and W.-C. Yang, *Sci. Rep.*, 2025, **15**, 16619.
23 M. Ashaduzzaman, M. A. Al Muhit, S. C. Dey, Md. M. Rahaman, H. N. Mahmudul Hasan, N. Mustary, Md. K. Hossain and M. K. Das, *Sci. Rep.*, 2025, **15**, 28288.
24 W. Ahmad, S. Ahmed and S. Kumar, *Int. J. Environ. Anal. Chem.*, 2025, **105**, 3309–3324.
25 B. I. Kharisov and O. V. Kharissova, *Synthesis at the Macroscale and Nanoscale*, Elsevier, Amsterdam Oxford Cambridge, 2021.
26 S. W. Balogun, H. O. Oyeshola, A. S. Ajani, O. O. James, M. K. Awodele, H. K. Adewumi, G. A. Àlàgbé, O. Olabisi, O. S. Akanbi, F. A. Ojeniyi and Y. K. Sanusi, *Heliyon*, 2024, **10**, e29452.
27 G. M. Abdelghani, A. B. Ahmed and A. B. Al-Zubaidi, *Sci. Rep.*, 2022, **12**, 20016.
28 M. A. Nazir, M. Hasan, G. Mustafa, T. Tariq, M. M. Ahmed, R. Golzari Dehno and M. Ghorbanpour, *Sci. Rep.*, 2024, **14**, 13091.
29 J. Jiang, J. Pi and J. Cai, *Bioinorg. Chem. Appl.*, 2018, **2018**, 1–18.
30 W. Ahmad and S. Kumar, *Emergent Mater.*, 2024, **7**, 1081–1090.
31 Y. Zheng, L. Fu, F. Han, A. Wang, W. Cai, J. Yu, J. Yang and F. Peng, *Green Chem. Lett. Rev.*, 2015, **8**, 59–63.
32 M. U. Munir, M. Ashraf, H. A. Abid, A. Javid, S. Riaz, H. Khanzada, A. Rehman and K. Iqbal, *J. Coat. Technol. Res.*, 2022, **19**, 467–475.
33 N. Chomchoei, P. Leelapornpisid, P. Tipduangta, P. Sangthong, P. Papan, B. Sirithunyalug and P. Samutrtai, *RSC Adv.*, 2023, **13**, 34987–35002.
34 K. Zeng, J. Li, Z. Zhang, M. Yan, Y. Liao, X. Zhang and C. Zhao, *J. Mater. Chem. B*, 2015, **3**, 5249–5260.
35 P. Sutradhar and M. Saha, *J. Exp. Nanosci.*, 2016, **11**, 314–327.
36 A. Abbas, S. Mansoor, M. H. Nawaz, A. A. Chaudhry, K. Ijaz, S. Riaz and A. Hayat, *RSC Adv.*, 2023, **13**, 11537–11545.
37 H. Ibrahim, V. Balédent, M. Impéror-Clerc and B. Pansu, *RSC Adv.*, 2022, **12**, 23675–23679.
38 C. Martín-Sánchez, A. Sánchez-Iglesias, J. A. Barreda-Argüeso, J. González and F. Rodríguez, *J. Mater. Chem. C*, 2024, **12**, 6469–6478.
39 N. Sharma, S. Jandaik, S. Kumar, M. Chitkara and I. S. Sandhu, *J. Exp. Nanosci.*, 2016, **11**, 54–71.
40 W. Ahmad, S. Ahmed, S. Kumar and H. C. Joshi, *Chem. Pap.*, 2024, **78**, 8309–8320.
41 H. Ahmad, A. B. Siddique, S. Zaheer, R. Sattar, A. Abbas, M. Amin, R. Al-Salahi, H. A. Abuelizz and M. Z. Saleem, *J. Water Proc. Eng.*, 2025, **74**, 107855.
42 N. Assad, A. Abbas, M. Fayyaz Ur Rehman and M. Naeem-ul-Hassan, *RSC Adv.*, 2024, **14**, 22344–22358.
43 A. K. Khajuria, A. Kandwal, R. K. Sharma, R. K. Bachheti, L. A. Worku and A. Bachheti, *Sci. Rep.*, 2025, **15**, 6541.
44 S. Ullah, M. Shaban, A. B. Siddique, A. Zulfiqar, N. S. Lali, M. Naeem-ul-Hassan, M. I. Irfan, M. Sher, M. Fayyaz Ur Rehman, A. Hanbashi, F. Y. Sabei, H. M. A. Amin and A. Abbas, *J. Environ. Chem. Eng.*, 2024, **12**, 113350.
45 A. Shoaib, S. Shahid, S. Mansoor, M. Javed, S. Iqbal, S. Mahmood, A. Bahadur, F. Jaber and M. Alshalwi, *Sci. Rep.*, 2024, **14**, 2499.
46 M. O. Lopes, A. Da Silva, C. Cerdeira, I. Ribeiro, I. Rosa, L. C. D. Reis, M. Da Silva, M. Marques, J. Chavasco and G. Da Silva, *Pharmacogn. Res.*, 2019, **11**, 1.
47 M. N. Alharthi, I. Ismail, S. Bellucci, N. H. Khdary and M. Abdel Salam, *Nanomaterials*, 2021, **11**, 1682.

48 H. Irfan, K. M. Racik and S. Anand, *J. Asian Ceram. Soc.*, 2018, **6**, 54–62.
49 D. Nath, F. Singh and R. Das, *Mater. Chem. Phys.*, 2020, **239**, 122021.
50 P. M. Kibasomba, S. Dhlamini, M. Maaza, C.-P. Liu, M. M. Rashad, D. A. Rayan and B. W. Mwakikunga, *Results Phys.*, 2018, **9**, 628–635.
51 Md. A. Samad Azad, Md. S. Hossain, S. P. Saikat, Md. R. Hasan and S. Bhowmik, *Nanoscale Adv.*, 2025, **7**(24), 8138–8153.
52 M. Y. Miah, S. Halder, S. P. Saikat, S. Dewanjee, Md. Ashaduzzaman and S. Bhowmik, *RSC Adv.*, 2025, **15**, 18971–18985.
53 M. F. Islam, S. Islam, M. A. S. Miah, A. K. O. Huq, A. K. Saha, Z. J. Mou, M. M. H. Mondol and M. N. I. Bhuiyan, *Heliyon*, 2024, **10**, e25430.
54 X. T. Tran, T. T. L. Bien, T. V. Tran and T. T. T. Nguyen, *Nanoscale Adv.*, 2024, **6**, 4885–4899.
55 A. E. Alprol, A. Eleryan, A. Abouelwafa, A. M. Gad and T. M. Hamad, *Sci. Rep.*, 2024, **14**, 32160.
56 M. Tashakkori Masuleh, M. Hasheminiasari and R. Ashiri, *Mater. Adv.*, 2025, **6**, 2611–2621.
57 N. J. Lakshmi, S. Anandakumar, V. Sampathkumar and S. Manoj, *Desalination Water Treat.*, 2024, **319**, 100557.
58 A. Solmaz, T. Turna and A. Baran, *Biomass Convers. Biorefin.*, 2024, **14**, 10771–10789.
59 G. Tizazu and E. Wondimu, *Anal. Sci. Adv.*, 2024, **5**, e2400023.
60 K. Davis, R. Yarbrough, M. Froeschle, J. White and H. Rathnayake, *RSC Adv.*, 2019, **9**, 14638–14648.
61 K. R. Ahammed, Md. Ashaduzzaman, S. C. Paul, M. R. Nath, S. Bhowmik, O. Saha, Md. M. Rahaman, S. Bhowmik and T. D. Aka, *SN Appl. Sci.*, 2020, **2**, 955.
62 M. Z. Khan, H. Taghavian, M. Fijalkowski, J. Militky, B. Tomkova, M. Venkataraman and K. Adach, *Colloids Surf., A*, 2023, **664**, 131135.
63 S. Raha and Md. Ahmaruzzaman, *Nanoscale Adv.*, 2022, **4**, 1868–1925.
64 A. R. Mendes, C. M. Granadeiro, A. Leite, E. Pereira, P. Teixeira and F. Poças, *Nanomaterials*, 2024, **14**, 638.
65 P. M. Kumar, R. Babujanarthanam, R. T. Selvi, R. Ganesamoorthy, S. J. J. Sudan, K. Kasthuri and R. Parameswari, *Appl. Phys. A*, 2025, **131**, 379.
66 A. Hussain, M. Oves, M. F. Alajmi, I. Hussain, S. Amir, J. Ahmed, M. T. Rehman, H. R. El-Seedi and I. Ali, *RSC Adv.*, 2019, **9**, 15357–15369.
67 M. Pozzi, S. Jonak Dutta, M. Kuntze, J. Bading, J. S. Rüßbült, C. Fabig, M. Langfeldt, F. Schulz, P. Horcajada and W. J. Parak, *J. Chem. Educ.*, 2024, **101**, 3146–3155.
68 M. Talha, A. S. Abbas, F. Jabeen, A. Hussain, I. Zahra, S. Aslam, I. Yousaf, M. Awais, M. B. Ali and A. Hedfi, *Waste Biomass Valorization*, 2025, DOI: 10.1007/s12649-025-03228-w.
69 J. Norooz Oliaee, M. Dehghany, A. R. W. McKellar and N. Moazzen-Ahmadi, *J. Chem. Phys.*, 2011, **135**, 044315.
70 C. Invernizzi, T. Rovetta, M. Licchelli and M. Malagodi, *Int. J. Anal. Chem.*, 2018, **2018**, 7823248.
71 J. Johnson, J. Mani, N. Ashwath and M. Naiker, *Spectrochim. Acta, Part A*, 2020, **233**, 118228.
72 A. M. A. Saputra, S. Gea, Andriayani, S. Sabar, R. Goei, M. Harsa, M. S. Harahap and Marpongahtun, *Next Mater.*, 2025, **9**, 101325.
73 Y. Sun, W. Zhang, Q. Li, H. Liu and X. Wang, *Adv. Sens. Energy Mater.*, 2023, **2**, 100069.
74 T.-H. Lai, C.-W. Tsao, M.-J. Fang, J.-Y. Wu, Y.-P. Chang, Y.-H. Chiu, P.-Y. Hsieh, M.-Y. Kuo, K.-D. Chang and Y.-J. Hsu, *ACS Appl. Mater. Interfaces*, 2022, **14**, 40771–40783.
75 A. B. Tegenaw, A. A. Yimer and T. T. Beyene, *Heliyon*, 2023, **9**, e20717.
76 S. K K, P. N. P M and M. Vasundhara, *RSC Adv.*, 2023, **13**, 1497–1515.
77 A. Modwi, M. A. Ghanem, A. M. Al-Mayouf and A. Houas, *J. Mol. Struct.*, 2018, **1173**, 1–6.
78 A. B. Siddique, M. A. Shaheen, A. Abbas, Y. Zaman, M. A. Bratty, A. Najmi, A. Hanbashi, M. Mustaqeem, H. A. Alhazmi, Z. U. Rehman, K. Zoghebi and H. M. A. Amin, *Heliyon*, 2024, **10**, e40679.
79 K. A. Isai and V. S. Shrivastava, *SN Appl. Sci.*, 2019, **1**, 1247.
80 H. Khan, M. Habib, A. Khan and D. C. Boffito, *J. Environ. Chem. Eng.*, 2020, **8**, 104282.
81 C. A. Soto-Robles, O. Nava, L. Cornejo, E. Lugo-Medina, A. R. Vilchis-Nestor, A. Castro-Beltrán and P. A. Luque, *J. Mol. Struct.*, 2021, **1225**, 129101.
82 H. Vahdat Vasei, S. M. Masoudpanah, M. Adeli, M. R. Aboutalebi and M. Habibollahzadeh, *Mater. Res. Bull.*, 2019, **117**, 72–77.
83 S. Ghaffar, A. Abbas, M. Naeem-ul-Hassan, N. Assad, M. Sher, S. Ullah, H. A. Alhazmi, A. Najmi, K. Zoghebi, M. Al Bratty, A. Hanbashi, H. A. Makeen and H. M. A. Amin, *Antioxidants*, 2023, **12**, 1201.
84 K. S. Ranjith and R. T. Rajendra Kumar, *RSC Adv.*, 2017, **7**, 4983–4992.